SUPPLEMENTARY INFORMATION
"Disentangling bulk and surface Rashba effects in ferroelectric α-GeTe"

J. Krempaský[1], H. Volfová[2], S. Muff[1,3], N. Pilet[1], G. Landolt[1,4],M. Radović[1,5], M. Shi[1], D. Kriegner[6], V. Holý[6], J. Braun[2], H. Ebert[2], F. Bisti[1], V.A. Rogalev[1], V.N. Strocov[1], G. Springholz[7],J. Minár[2,8], J. H. Dil[1,3]

[1]*Swiss Light Source, Paul Scherrer Institut, CH-5232 Villigen PSI, Switzerland*

[2]*Department of Chemistry, Ludwig Maximillian University, 81377 Munich, Germany*

[3]*Institute of physics, Ecole Polytechnique Fédérale de Lausanne, CH-1015 Lausanne, Switzerland*

[4]*Physik-Institut, Universität Zürich, Winterthurerstrasse 190, 8057 Zürich, Switzerland*

[5]*SwissFEL, Paul Scherrer Institut, CH-5232 Villigen PSI, Switzerland*

[6]*Department of Condensed Matter Physics, Charles University in Prague, Ke Karlovu 5, 121 16 Praha 2, Czech Republic*

[7]*Institut für Halbleiter-und Festkörperphysik, Johannes Kepler Universität, A-4040 Linz, Austria*

[8]*New Technologies-Research Center University of West Bohemia, Plzeň, Czech Republic*

I. THE α-GETE(111) SURFACE

A. Low energy and reflection high energy electron diffraction.

Panel (a) in Figure S1 characterizes the sample surface by *in-situ* low-energy electron diffraction (LEED) after complete decapping; and panel (b) by reflection high-energy electron diffraction (RHEED). A lack of surface reconstruction in LEED and the presence of Kikuchi lines in RHEED indicate superior quality α-GeTe(111) surface and epilayers.

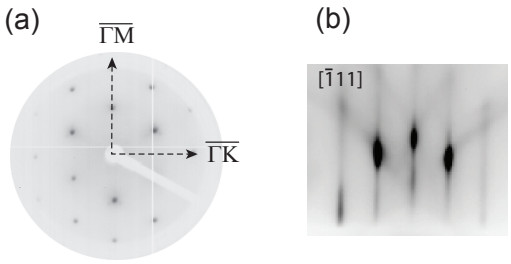

FIG. S1. **α-GeTethin film epilayers. (a)** LEED. **(b)** RHEED.

B. α-GeTe(111) Ge- vs. Te-terminated surface calculation

In order to understand the surface termination, we compare our ARPES data with one-step fotoemission calculations (1SM) in which we model the semi-infinite crystal surface termination with Te- and Ge-surface atoms, respectively. As seen in Figure S2, the Te-terminated model predicts electron-like band dispersion near E_F. On the other hand the Ge-terminated surface forms hole-like surface states near E_F. Referring to the experimental band map in Figures 2 and 3 in the main text it is evident that the α-GeTe is Te-terminated (111), which is also found to be energetically more favorable [1].

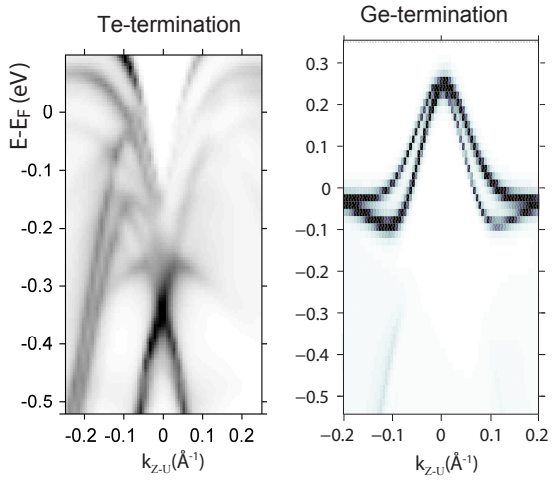

FIG. S2. **One-step ARPES calculation** for tellurium (left) and germanium (right) terminated α-GeTe(111) surface.

II. α-GETE(111)/BAF_2 CHEMICAL, STRUCTURAL AND FERROELECTRIC CHARACTERIZATION.

A. Te($4d$) and Ge($3d$) core-levels in X-ray photoelectron spectroscopy.

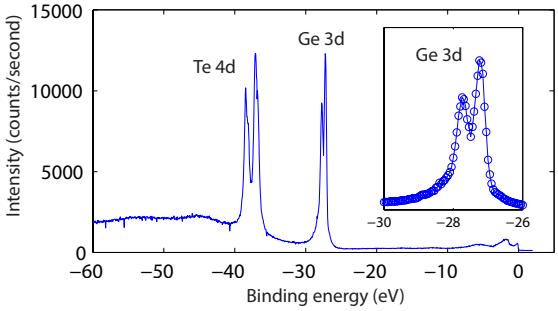

FIG. S3. **in X-ray photoelectron spectroscopy.** Shallow core levels from uncapped α-GeTe surface showing peaks from Te($4d$) and Ge($3d$) states measured with the channeltron detectors of the COPHEE SARPES set-up at hν=120 eV. The inset shows a zoom into the Ge($3d_{5/2}$) and Ge($3d_{3/2}$).

A protective stack of amorphous Te- and Se-capping layers with a total thickness of 20 nm was used to avoid surface degradation and oxidation. At moderate annealing temperatures $< 200°$C the surface remains Te-capped with a residual cap thickness of around 0.5–1 nm, whereas annealing at higher temperatures yields a completely uncapped GeTe surface. Figure S3 shows X-ray photoelectron spectroscopy (XPS) data measured at a photon energy of 120 eV with p-polarized light. The core levels from Te($4d$) and Ge($3d$) are without any oxidation satellite features. This indicates that the surface preparation by removing the protective amorphous Te-cap avoided surface oxidation and degradation. Hence ARPES data in the main text reflect intrinsic α-GeTe(111) properties.

B. Structural characterization and bulk ferroelectricity.

GeTe is probably the simplest ferroelectric material consisting only of two kinds of atoms per unit cell. At high temperatures it crystallizes in the cubic rock salt structure but undergoes a spontaneous ferroelectric phase transition at a Curie temperature of around 700 K [2, 3], below which the *Fm3m* cubic symmetry is broken. Consequently a ferroelectric rhombohedral *R3m* $\alpha-$structure is formed by an elongation and contraction of the unit cell along a $\langle 111 \rangle$ direction. This is accompanied by a large displacement of the Ge and Te sublattices relative to each other in the $\langle 111 \rangle$ direction, inducing a ferroelectric dipole moment along the distortion direction denoted by orange arrows in Fig. S4a. In bulk GeTe the eight possible $\langle 111 \rangle$ distortion directions are equivalent. Thus, a multi-domain structure is formed with ferroelectric dipole moments randomly oriented in any of the equivalent $\langle 111 \rangle$ directions [3]. In addition, the effect of the ferroelectric dipoles on the band structure is predicted to be largest near the Z-point of the Brillouin zone located along the $\langle 111 \rangle$ **k**-space direction [4]. This requires the preparation of α-GeTe crystals with (111) orientation, which however, like all other IV-VI compounds, cleave preferentially in non-polar (100) direction. This can be resolved by using epitaxial α-GeTe(111) layers in which due to strain and interface effects, nearly single domain films with the ferroelectric domains aligned in the [111] surface normal direction can be prepared [5, 6]. This is illustrated by the x-ray reciprocal space map of our GeTe layers grown on BaF_2(111) depicted in Fig. S4b, exhibiting a 30 times higher intensity of the [111] domains than those of the oblique $\langle \bar{1}11 \rangle$ domains. The temperature dependent lattice distortion shown in Fig. S4c shows a Curie temperature of 700 K for the layers. In experiments based on extended X-ray absorption fine structure measurements (Fig. S4d) a rhombohedral distortion angle of 88.2° and a Ge/Te sublattice displacement as high as ≈0.31 Å at 15 K is obtained, in excellent agreement with the bulk material [2, 3]. The relative shift of the Te and Ge sublattices are evidenced by the splitting of the peaks at a radial distance of ≈3 Å, which is not present in the cubic phase. The data was obtained at the XAS beamline at the Synchrotron Light Source ANKA in fluorescence mode. Spectra were fitted using *Artemis* [7] and *Mkfit* [8], which allow determination of the atomic positions from the EXAFS data. The best fit is represented by the solid lines evidencing the agreement with the experimental data. In our thin α-GeTe(111) film such a shift is inducing a collective FE-order along the $\langle 111 \rangle$ direction perpendicular to the sample surface which we investigated with Piezo-Force-Microscopy.

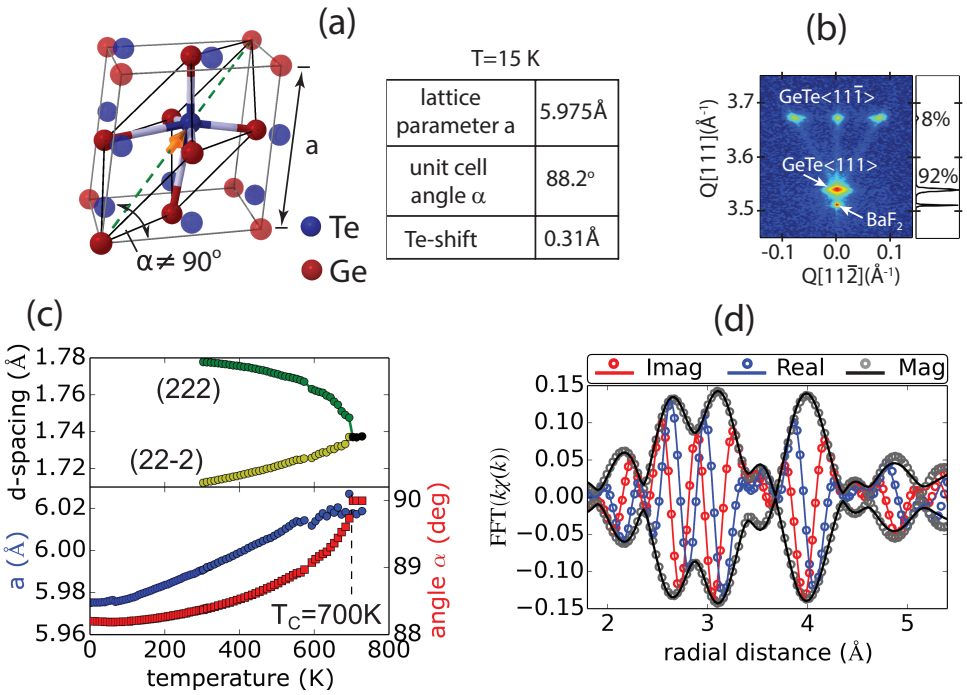

FIG. S4. **α-GeTe(111)/BaF_2 structural characterization and bulk ferroelectricity**. Rhombohedral lattice distortion and off-center ferroelectric sublattice displacement of GeTe. **(a)** Unit cell of GeTe in the rhombohedral ferroelectric phase below the Curie temperature T_C= 700K. In the ferroelectric phase, the Ge- and Te-sublattices are displaced with respect to each other along the [111] direction as indicated by the orange arrow. (b) Room temperature (222) reciprocal space map of the GeTe epilayer on BaF_2 (111) revealing a splitting of the GeTe Bragg reflection into four peaks due to the multi-domain ferroelectricity, with the main ferroelectric domain perpendicular to the epilayer (92% of the film volume). **(c)** Temperature dependence of the lattice parameters a and the lattice spacing of the (222) and (22$\bar{2}$) Bragg peaks, showing the para/ferroelectric transition at 700K and the strong increase of lattice distortion with decreasing temperature. A table lists the structural paramenters at 15 K. **(d)** r-space FFT{k[χ(k)]} EXAFS data obtained from the Ge-K edge at T=15K. Shown are the real and imaginary, as well as the magnitude of the Fourier transform of k[χ(k)] of the experimental data (open circles) together with a fit to the data (solid lines), giving a shift of the Te sublattice of 0.31 Å as listed in the table.

C. α-GeTe surface ferroelectric characterization

Because α-GeTe(111) grown on BaF_2 precludes piezoelectric-force-microscopy (PFM) measurement due to the highly isolating properties of the substrate, the PFM was performed on thin films grown on and InP(111) substrate. The PFM measurements were performed at the Swiss Light Source NanoXAS beamline [9]. Figure S5 shows the PFM amplitude and phase contrast of domains poled by applying a voltage on the AFM tip and keeping the sample grounded.

The PFM setup is sensitive only to the out-of-plane component of the polarization. The local PFM data from Fig. S5a,b show characteristic "butterfly" shape in amplitude and hysteretic shape in phase signal. Due to hysteretic effects, a domain written onto a pre-existing domain shows a lower PFM amplitude, indicated in orange region of Fig. S5c,d. The poled regions with opposite voltage (±4 V) show a phase difference of 180° suggesting full polarization reversal consistent with already investigated α-GeTe(111) grown on Si(111) [10]. However, the polarization reversal in our case needs factor 10 smaller voltages presumably because the InP lattice is reducing the strain effects inside the GeTe thin film.

III. SPIN ANALYSIS OF THE α-GETE(111) SURFACE AND BULK ELECTRONIC STRUCTURE.

A. Identifying the α-GeTe surface resonance states.

The *ab initio* calculations are based on density functional theory as implemented within the multiple scattering theory [11, 12] including the spin-orbit coupling. As a first step of our investigations we performed self-consistent

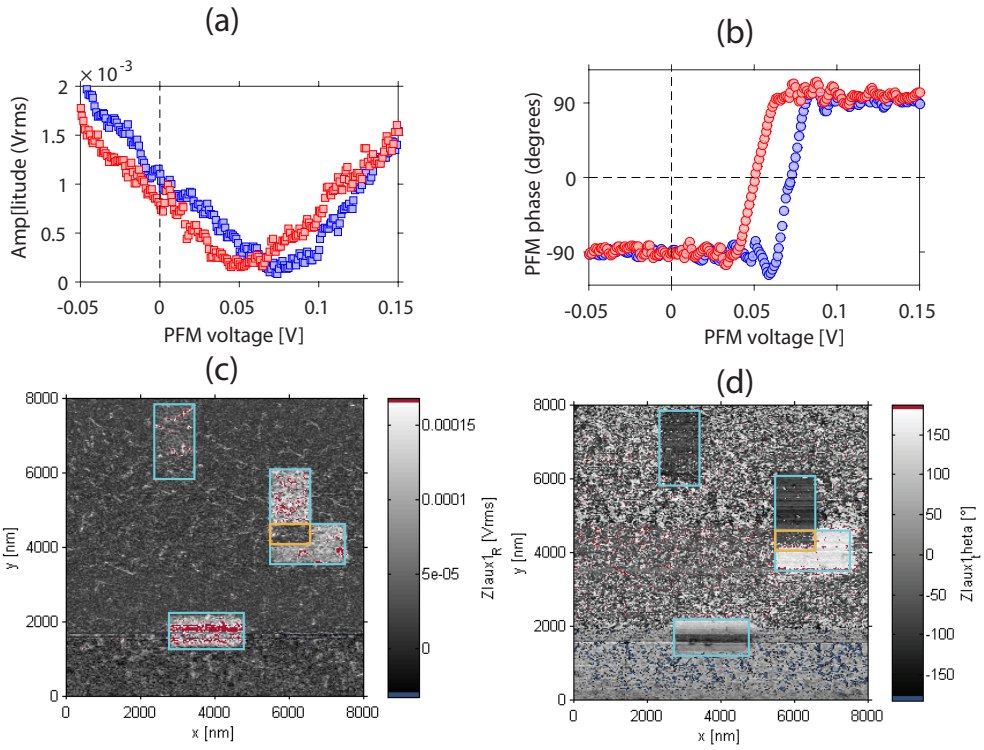

FIG. S5. **Piezo-Force-Microscopy (PFM)**. **(a)** PFM amplitude and **(b)** phase signals, with corresponding false color plots in **(c,d)**. The regions denoted by blue rectangles are biased by applying ±4V bias voltage. Orange regions indicate overwritten ferroelectric domain.

calculations for 3D bulk as well as 2D semi-infinite surface of α-GeTe(111) within the screened Korringa-Kohn-Rostoker formalism [12]. The corresponding ground state band structures are presented in terms of Bloch spectral functions (BSF). These self-consistent results served as an input for our spectroscopic investigations. The ARPES calculations were performed in the framework of the fully relativistic one-step model (1SM) of photoemission[13, 14] in its spin-density matrix formulation[15], which accounts properly for the complete spin-polarization vector, in particular for Rashba systems like GeTe. Together with a realistic model for the surface barrier potential, 1SM calculations based on a semi-infinite half-space configuration were decisive to substantiate the α-GeTe(111) surface-generated spectral features on both qualitative and quantitative levels. Ground state, as well as 1SM calculations of Te-terminated semi-infinite surface include the intrinsic p-type doping due to Ge vacancies by means of coherent potential approximation (CPA) alloy theory.

Fig. 2f,g,h of the main text show the layer-resolved BSF calculations, where selected areas identify decay lengths characteristic for pure bulk, surface resonances, and pure surface states. The ARPES response of the valence electron states critically depends on the final-state and matrix-element effects, the 1SM calculations is a complementary approach to disentangle these states in terms of their bulk-like or surface-related character. We demonstrate that both approaches give consistent results, which is important for a correct description of the states in the α-GeTe(111) surface electronic structure.

Within the 1SM approach the calculated surface electronic structure can be quantified using the 1SM determinant [13, 16]. It measures the reflection of the electron states from the crystal bulk which directly relates to the degree of their surface localization. To compare with the ground state BSF semi-infinite calculations, Fig. S6 compares the ARPES (panel a) and SARPES (panel b) band maps with the 1SM determinant in panel c which we plot in a logarithmic color scale. Small values (white to light yellow colours) correspond to surface states with the maximum of their wave functions between the first atomic layer and vacuum (highly localized states), whereas pure bulk states have determinant values close to one and are represented in black (delocalized states). In-between the two extreme cases, a variety of surface resonance states (SR) are found characterized by intermediate determinant values. These bulk-derived states, represented by orange-red shades, are resonantly enhanced at the surface and extend over large distances toward the bulk asymptotics, as also sketched in the Fig. 2h of main text. The transitions between all states appear gradually, but as a whole the SR form the primary spectral weight dispersing across the narrow gap, forming

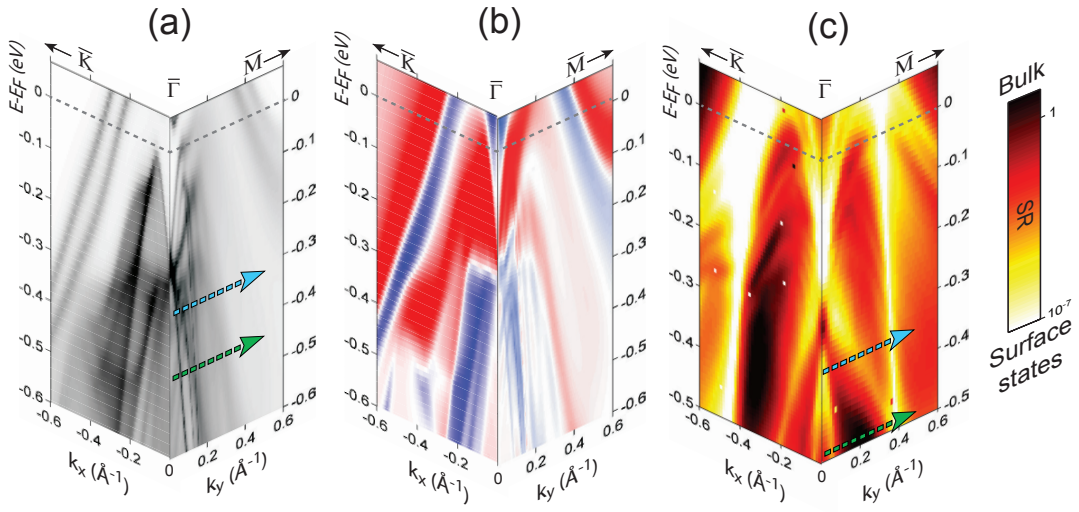

FIG. S6. **α-GeTe surface electronic structure calculations.** **(a)** Spin-integrated and **(b)** spin-resolved Bloch spectral functions from a semi-infinite surface. **(c)** Logarithmic false color map of ARPES 1SM-determinant values indicating the bulk (black shades), surface (white-yellow shades) and surface-resonances in red-orange shades. The green arrow indicate binding energy with momenta where the bulk Rashba splitting is best observed, the blue arrow shows where the bulk Rashba splitting hybridize with surface resonances.

metallic states at E_F, and becoming degenerate with bulk Rashba bands at higher binding energies. In ARPES band maps they form SR-replicas of the pure bulk states, as seen in Fig. 3 of the main text. They are quenched on Te-capped samples, confirming their surface-related character.

In order to correctly interpret the data, the SR-replicas need to be disentangled from the pure bulk state in SARPES measurements. The 1SM determinant in Fig. S6c suggests that for binding energies around 0.5 eV there is an ideal locus of **k**-space momenta (indicated by the green arrow), which should unambiguously identify pure bulk states surrounded by surface-resonance states with higher momenta. For lower binding energies (light-blue arrow in Fig. S6c) the bulk states start to hybridize with the SR-states with less steep dispersive trend compared to bulk bands, which we also directly observe in SX-ARPES (arrows in Fig. 2e,f of the main text). Below we show that despite this evident hybridization they still retain the characteristic canted spin arrangement of bulk states.

B. SARPES 3D-vectorial peak-fitting analysis

The COPHEE experimental station at the Swiss Light Source is a unique facility for SARPES experiments with a 3D Mott polarimeter[17, 18]. Combined with an angle-resolving photoelectron spectrometer it produces complete data sets consisting of photoemission intensities as well as spin polarization curves for three orthogonal vector components. SARPES data in the main text show the populations of electrons with momentum along $\overline{\mathrm{K\Gamma K}}$ and $\overline{\mathrm{M\Gamma M}}$ having their spin parallel (up) or antiparallel (down) to the local momentum-dependent spin quantization axis. To ensure equivalent measurement conditions, data were taken by tilting the sample [the τ direction seen in Fig. S7] with $\overline{\Gamma\mathrm{K}}$ or $\overline{\Gamma\mathrm{M}}$ oriented perpendicular to the scattering plane. In a well established fitting routine [19] the total intensity photoemission momentum distribution curves (MDC) are first dissected into individual Voigt function peaks and a background. The polarization curves are modelled until the best fit is reached by simultaneously fitting the MDC intensity and the polarizations P_x, P_y and P_z. This way a spin polarization vector is assigned to each peak. From the total intensities I_{tot} and the polarization data we generate the spin-resolved populations I_x, I_y and I_z along the three coordinate axes as a function of electron momenta as

$$I_i^{\uparrow,\downarrow} = I_{tot}(1 \pm P_i)/2$$

We now concentrate on locating by UV-ARPES the Z-point in **k**-space where the Rashba splitting is most pronounced. In the ΓZU Brillouin zone (BZ) plane the corresponding band-maps measured for different photon energies are shown in Fig. S7c. In this data a dispersive bulk 3D-Rashba splitting is readily identified by the Dirac point at Γ and band extrema at finite momenta. We find that the Z-point in the bulk BZ is located at hν=22($\pm$0.5) eV where

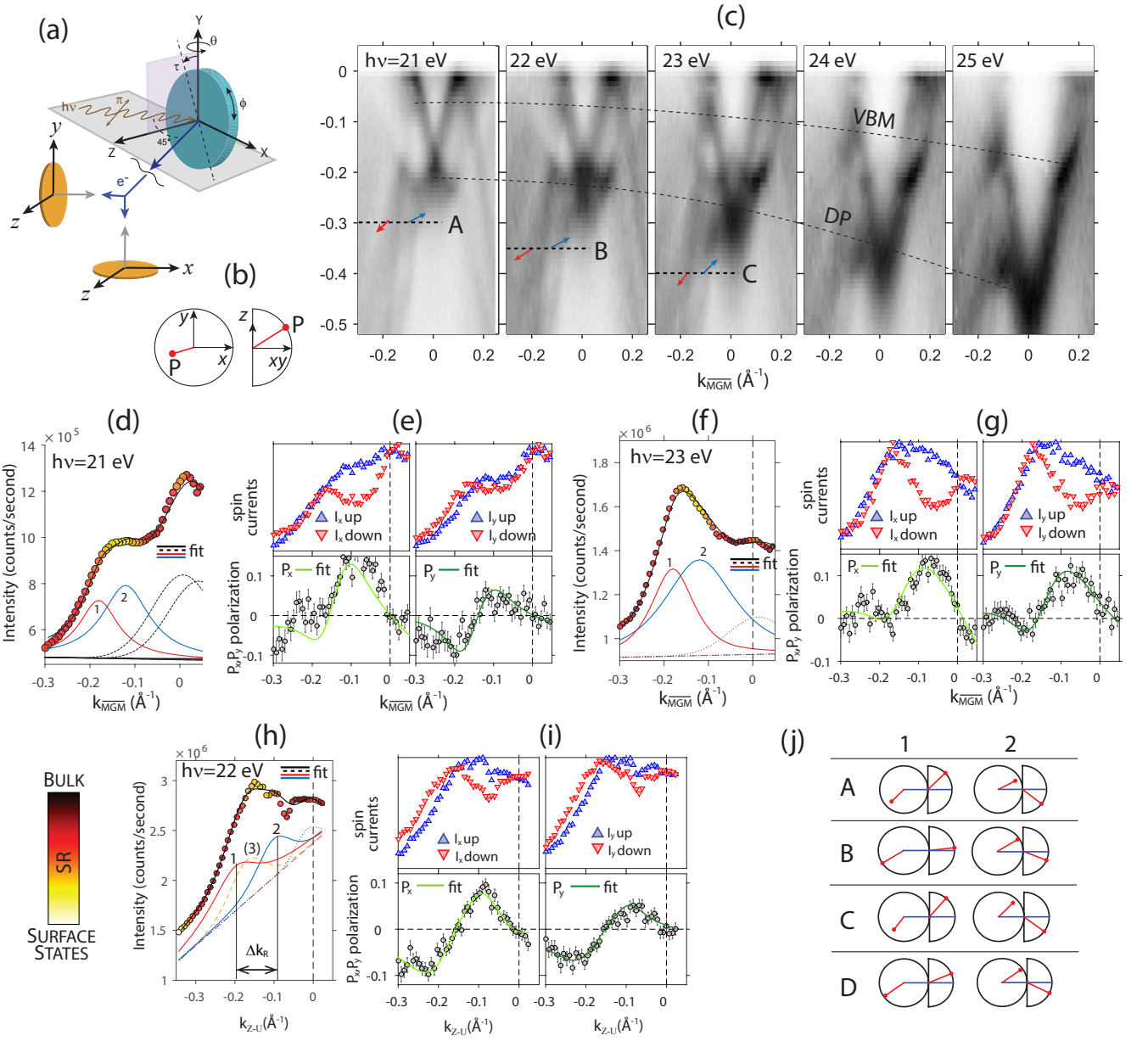

FIG. S7. **3D vectorial spin analysis of bulk Rashba properties. (a)** Experimental geometry of the (S)ARPES experiment with π-polarized light and local {xyz} axes measuring the 3D-polarization with corresponding definition of the polar representation of the 3D spin vectors (red ball-pointed arrows) in **(b)**. **(c)** ARPES data for selected hν measured in the Z-U plane. Dashed lines highlight the dispersion of the Dirac point (DP) along with the top of the valence band (VBM). **(d)** SARPES data and spin-fits **(e)** measured along $\overline{\mathrm{M\Gamma M}}$ for a photon energy of 21 eV, **(f,g)** 23 eV and **(h,i)** 22 eV. **(j)** Summary of the bulk Rashba split bands 1–2 from cuts A-B-C indicated in (c), compared to data from Fig.4i of the main text (cut D).

the Dirac point has a minimum binding energy of 0.25 eV, in agreement with SX-ARPES data in Fig. 2c-e of the main text. Because the spin-polarization can be photon-energy dependent, the canted spin orientation of the bulk bands was verified for several photon energies. Taking into account the dispersive Dirac point, SARPES data with the $P_{x,y}$ fits seen in Fig. S7d-i are summarized in panel j. Since the different sets of measurements are compatible with each other and settle the 3D-fits with the same in-plane canted spin arrangement for peaks 1–2 with the same modulation of the P_z, we conclude that our data unambiguously backtrace the measured spin signal to the bulk Rashba splitting of the initial states, as predicted in Fig. 4a of the main text.

Finally we discuss the in-plane spin texture at the Fermi energy from Fig. 4e of the main text. Ten peaks are needed for the fit in both the $\overline{\mathrm{K\Gamma K}}$ and $\overline{\mathrm{M\Gamma M}}$ direction. Figure S8(c) shows the resulting cochiral counterclockwise

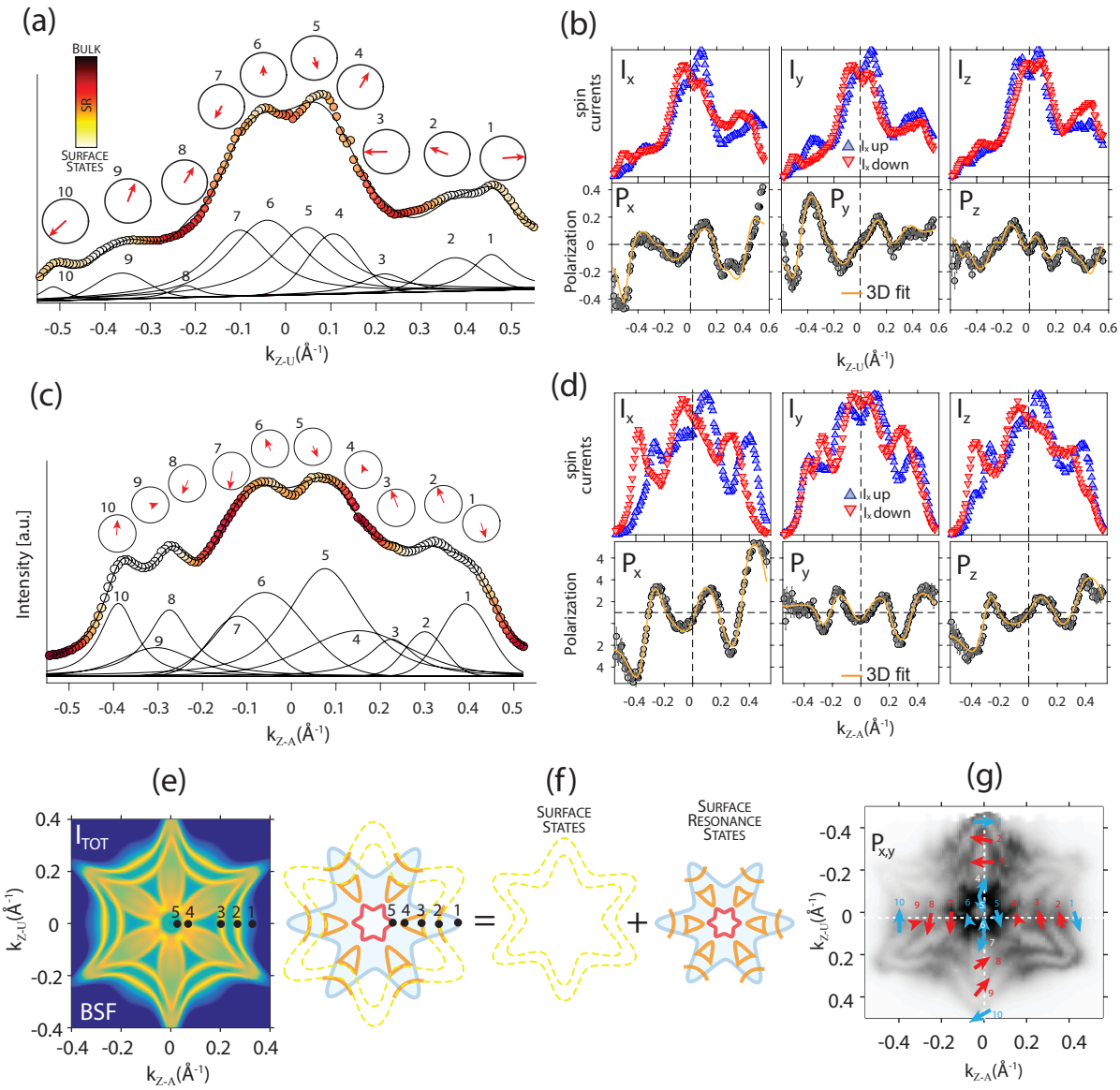

FIG. S8. **3D vectorial spin analysis at E_F along $\overline{M\Gamma M}$. (a,b)** and $\overline{K\Gamma K}$ **(c,d)**. The total intensity fit (a,c) consist of 10 Voigt functions. The corresponding spin currents I_x, I_y and I_z and P_x, P_y and P_z polarizations including fits are seen in (b,d). (e) Theoretical Fermi surface map with the anatomy sketched in (f). (g) Experimental FSM with $P_{x,y}$ spinors taken from the spin-fits in panels a and c superimposed

spin helicity displayed by red arrows in Fig. 4e, and the clockwise helicity displayed by blue arrows. Despite the overall complexity of the spin texture, within the experimental resolution limitation ($\approx 0.05 Å^{-1}$ at 22 eV), each band indicate opposite spin orientations at opposite Fermi momenta. We conclude that the spin-momentum locking is causing a complex trivial spin texture due to surface resonance effects, constituting the peaks 2-3-4 and 7-8-9 in both $\overline{\Gamma K}$ and $\overline{\Gamma M}$ directions. Finally, Fig. S8e-f shows that the anatomy of the surface electronic structure consists of surface and SR-states with stars rotated by 30°. By quenching these states the texture reduces to a typical bulk Rashba arrangement as seen in Fig. 2c of the main text.

[1] Deringer, V. L., Lumeij, M. & Dronskowski, R. Ab Initio Modeling of α-GeTe(111) Surfaces. *The Journal of Physical Chemistry C* **116**, 15801–15811 (2012).

[2] Chattopadhyay, T., Boucherle, J. X. & von Schnering, H. G. Neutron diffraction study on the structural phase transition in GeTe. *Journal of Physics C: Solid State Physics* **20**, 1431–1440 (1987).

[3] Jantsch, W. (ed.) *Dielectric Properties and Soft Modes in Semiconducting (Pb, Sn, Ge)Te* (Springer Tracts in Mod. Phys. 99, Springer Verlag, Berlin 1983, 1979).

[4] Di Sante, D., Barone, P., Bertacco, R. & Picozzi, S. Electric Control of the Giant Rashba Effect in Bulk GeTe. *Advanced Materials* **25**, 509–513 (2013).

[5] Przybylińska, H. *et al.* Magnetic-Field-Induced Ferroelectric Polarization Reversal in the Multiferroic $Ge_{1-x}Mn_xTe$ Semiconductor. *Phys. Rev. Lett.* **112**, 047202 (2014).

[6] Kolobov, A. V. *et al.* Ferroelectric switching in epitaxial GeTe films. *APL Materials* **2** (2014).

[7] Ravel, B. & Newville, M. ATHENA, ARTEMIS, HEPHAESTUS: data analysis for X-ray absorption spectroscopy using IFEFFIT. *J. Synchro. Rad.* **12**, 537–41 (2005).

[8] Kelly, S. D., Stern, E. A. & Ingalls, R. Determining crystalline atomic positions using XAFS, a new addition to the UWXAFS analysis package. *J. Synchro. Rad.* **8**, 311 (2001).

[9] Pilet, N. *et al.* Nanostructure characterization by a combined x-ray absorption/scanning force microscopy system. *Nanotechnology* **23**, 475708 (2012). URL `http://www.ncbi.nlm.nih.gov/pubmed/23117254`.

[10] Liebmann, M. *et al.* Giant Rashba-Type Spin Splitting in Ferroelectric GeTe(111). *Advanced Materials* **28**, 560–565 (2016).

[11] Ebert, H. *et al*. (2014) Munich SPR-KKR package, version 7.2, http://olymp.cup.uni-muenchen.de: /ak/ebert/SPRKKR.

[12] Ebert, H., Ködderitzsch, D. & Minár, J. Calculating condensed matter properties using the KKR-Green's function method–recent developments and applications. *Rep. Prog. Phys.* **74** (2011).

[13] Braun, J. & Donath, M. Theory of photoemission from surfaces. *J. Phys.: Condens. Matter* **16**, 2539–2555 (2004).

[14] Ebert, H. *Electronic Structure and Physical Properties of Solids, Lecture Notes in Physics*, vol. 535 (Springer-Verlag Berlin Heidelberg, 2000).

[15] Braun, J. *et al.* Exceptional behavior of d-like surface resonances on W(110): the one-step model in its density matrix formulation. *New Journal of Physics* **16**, 015005 (2014).

[16] Echenique, P. M. & Pendry, J. B. The existence and detection of rydberg states at surfaces. *J. Phys. C: Solid State Phys.* **11**, 2065–2075 (1978).

[17] Hoesch, M. *et al.* Spin-polarized Fermi surface mapping. *J. Electron Spectrosc. Relat. Phenom.* **124**, 263–279 (2002).

[18] Dil, J. H. Spin and angle resolved photoemission on non-magnetic low-dimensional systems. *J. Phys.: Condens. Matter* **21**, 403001 (2009).

[19] Meier, F., Dil, J. H. & Osterwalder, J. Measuring spin polarization vectors in angle-resolved photoemission spectroscopy. *New J. Phys.* **11**, 125008 (2009).